Detection of low-energy electrons with transition-edge sensors

(Article begins on next page)

22 February 2025

Detection of low-energy electrons with transition-edge sensors

Carlo Pepe,[1,2] Benedetta Corcione,[3,4] Francesco Pandolfi,[4,*] Hobey Garrone,[1,2]
Eugenio Monticone,[1] Ilaria Rago,[4] Gianluca Cavoto,[3,4] Alice Apponi,[5] Alessandro Ruocco,[5]
Federico Malnati,[6] Danilo Serazio,[1] and Mauro Rajteri[1]

[1] *Istituto Nazionale di Ricerca Metrologica, Strada delle Cacce 91, Torino 10135, Italy*
[2] *Dipartimento di Elettronica e Telecomunicazioni, Politecnico di Torino, Corso Duca degli Abruzzi 24,*
Torino 10129, Italy
[3] *Sapienza Università di Roma, Piazzale Aldo Moro 2, Rome 00185, Italy*
[4] *Istituto Nazionale di Fisica Nucleare - Sezione di Roma, Piazzale Aldo Moro 2, Rome 00185, Italy*
[5] *Dipartimento di Scienze Università degli Studi Roma Tre, Istituto Nazionale di Fisica Nucleare - Sezione di*
Roma Tre, Via della Vasca Navale 84, Rome 00146, Italy
[6] *Dipartimento di Fisica, Università di Torino, via Pietro Giuria 1, Torino 10125, Italy*

We present the detection of electrons with kinetic energy in the 100 eV range with transition-edge sensors (TESs). This has been achieved with a (100×100)-μm^2 Ti/Au bilayer TES, with a critical temperature of about 84 mK. The electrons are produced directly in the cryostat by an innovative cold source based on field emission from vertically aligned multiwall carbon nanotubes. We obtain a Gaussian energy resolution between 0.8 and 1.8 eV for fully absorbed electrons in the (90–101) eV energy range, which is found to be compatible with the resolution of this same device for photons in the same energy range. This work opens possibilities for high-precision energy measurements of low-energy electrons.

Transition-edge sensors (TESs) are highly sensitive microcalorimeters capable of high-resolution single-photon counting across a wide energy spectrum [1,2]. The detection scheme is based on the absorption of photons in a thin superconducting film, in which their energy is transformed into heat. By operating a TES at its critical temperature T_C, even small variations in temperature lead to measurable changes in its electrical resistance, owing to the steep transition between the superconducting regime and the normal-conduction one. TES devices have been capable of achieving single-photon Gaussian energy resolutions below 50 meV for 0.8-eV photons [3,4].

In principle, this detection scheme should also be sensitive to electrons absorbed in the superconducting film. However, there is currently very limited research on TES electron detection, except for a recent result [5] for electrons in the 300–2000 eV energy range, which achieves a Gaussian energy resolution $\sigma_e > 17$ eV. Low-energy electrons have been detected using various devices, such as microchannel plates [6], which suffer from poor energy resolution and geometrical inefficiencies due to their nonunitary fill factor. Silicon-based detectors, including avalanche photodiodes [7] and silicon drift detectors [8], face challenges such as dead layers at the detector entrance, where low-energy electrons are absorbed before producing a signal.

In contrast, TES devices offer a detection scheme that, in principle, is free of dead layers and features a unitary fill factor, providing the potential for high efficiency and excellent intrinsic energy resolution. These features make this technology potentially very interesting for low-energy electron spectroscopy [5], microcalorimetry [9,10], and for experiments studying β-decay and neutrino physics. One example is the PTOLEMY project, which aims to detect the cosmic neutrino background by analyzing the endpoint of the β^- decay of tritium, seeking to achieve an electron energy resolution of 50 meV for 10-eV electrons [11–13].

In this work, electrons are produced by field emission from vertically aligned carbon nanotubes (CNTs). This innovative cold-source solution overcomes the issues in interfacing standard hot-filament-based electron sources with the TES working at cryogenic temperature, thus allowing the source to be placed directly inside the cryostat, close to the TES.

*Contact author: francesco.pandolfi@roma1.infn.it

The results presented in the following were obtained in the Innovative Cryogenic Detectors Laboratory of Istituto Nazionale di Ricerca Metrologica (INRiM) in Torino (Italy) [14]. The TES detector operates inside an adiabatic demagnetization refrigerator cryostat, at a stable bath temperature $T_{bath} = 41.7 \pm 0.2$ mK, as measured by a ruthenium oxide thermal sensor. To suppress magnetic interference affecting the electrons in motion, TESs, and dc SQUIDs (superconducting quantum interference devices), a cryogenic magnetic shield is installed around the working area within the cryostat.

A schematic view of the layers that compose the TES and its surroundings is shown in Fig. 1(a). The TES device used in this work was fabricated at QR Lab, INRiM, has an area of (100×100) μm^2, and is a Ti/Au bilayer device, composed of a 15-nm layer of titanium covered by a 30-nm layer of gold, deposited by thermal evaporation on a silicon substrate covered by 150 nm of SiO_2 and 500 nm of SiN_x on both sides [15]. The wiring is done with 50-nm superconducting niobium strips, deposited on the substrate via sputtering. The TES has a critical temperature $T_C = 84$ mK and is characterized in the (3–140) eV energy range with 406-nm photons from a pulsed laser. By varying the laser intensity, the number of photons per bunch N_γ can be adjusted. The result of this characterization, in the energy range of interest for this work, is shown in Fig. 2: the peaks corresponding to $30 \leq N_\gamma \leq 34$ are clearly distinguishable, and fitted with a sum of Gaussian functions. The
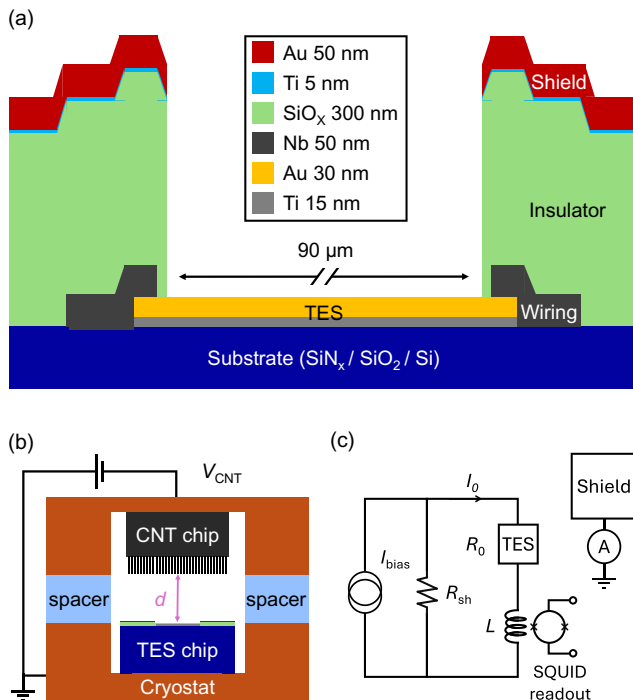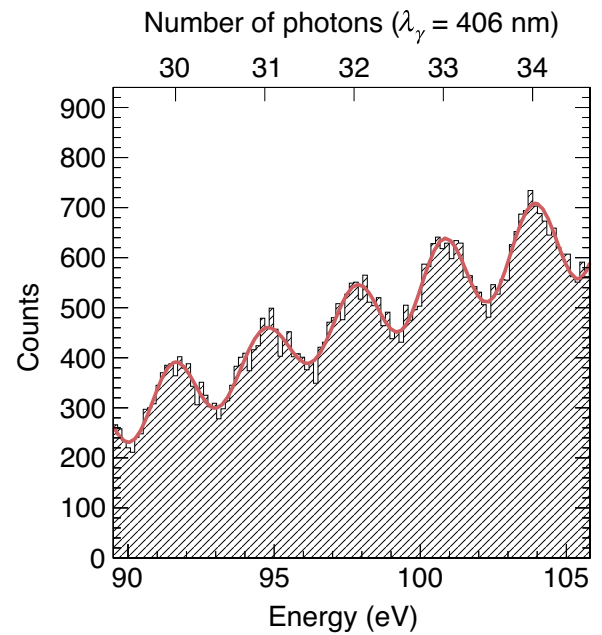

FIG. 2. TES optical characterization with $\lambda_\gamma = 406$-nm photons. The histogram of the pulse amplitudes reports peaks corresponding to $30 \leq N_\gamma \leq 34$, which are clearly distinguishable, and fitted with a sum of Gaussian functions (red line).

FIG. 1. (a) Schematic view of the TES device and its shield layer (*y* axis to scale, *x* axis not to scale). (b) Schematic view of the setup. (c) Schematic view of the electrical circuit.

dark count of the TES is found to be negligible compared with the signal rate with the trigger threshold used in this work, as expected from this type of device [16].

This TES is adapted for electron detection by adding a shield layer, which is needed as the electron source has a significantly larger area compared with the TES. The shield leaves the TES active area exposed, but covers the area surrounding it, as direct electron hits on the wiring would induce electrical noise, and hits on the insulating substrate would lead to charge build-up. The shield layer is produced by thermal evaporation, depositing an insulating layer consisting of 300 nm of amorphous silicon oxide (SiO_x) [17], followed by a thin (5-nm) layer of titanium, and finally a 50-nm layer of gold. The titanium layer is necessary for best adhesion of gold to the SiO_x.

The electron source consists of a sample of vertically aligned multiwall CNTs synthesized in the INFN laboratory "TITAN" at Sapienza University of Rome [18–21]. The nanotubes are grown through chemical vapor deposition on a 500-μm silicon substrate, and cover a surface of roughly (3×3) mm^2. Because of the high geometrical field enhancement factor of their tips, nanotubes are capable of emitting electrons through quantum tunneling (field emission) without the necessity of very high voltages [22–25]. Furthermore, field emission does not generate heat and can therefore be used in a cryostat.

The TES and the nanotubes are placed on two copper plates, facing each other, separated by 0.5-mm sapphire

spacers, which ensure electrical insulation while guaranteeing a good degree of thermal conductance. The top copper plate, where the nanotubes are hosted, is provided with a negative voltage V_{CNT} to induce field emission. The bottom plate is in thermal contact with the cryostat and electrically grounded through it. The distance between the tips of the nanotubes and the surface of the TES is $d = 600 \pm 50 \, \mu m$. A schematic view of the setup is shown in Fig. 1(b).

In field emission electrons tunnel through the potential barrier, and are therefore emitted at a potential ϕ_{CNT} below the vacuum level, where ϕ_{CNT} is the work function of the CNTs [26]. Additionally, the difference between the work functions of the CNTs and the TES will create an effective field that will further correct the kinetic energy of the electrons E_e. In the form of a formula:

$$E_e = eV_{CNT} - \phi_{CNT} + (\phi_{CNT} - \phi_{TES}) = eV_{CNT} - \phi_{TES}, \quad (1)$$

where e is the elementary charge. The TES work function is measured with ultraviolet photoemission spectroscopy in Roma Tre University's LASEC lab, obtaining $\phi_{TES} = 4.38 \pm 0.03$ eV. Moreover, the source is monochromatic, as the energy spread of the field-emitted electrons is negligible with the values of temperature and electric field of our setup [27].

The electron emission from the CNTs is measured in two different ways, as shown in the electrical circuits in Fig. 1(c): by connecting a Keithley 6487 picoammeter to the metallic shield layer, to measure the current I_{CNT}; and by counting the signals in the TES, while operating it at a working point of $R_0 = 0.35 R_N$, where $R_N = 246$ mΩ is the resistance of the TES in its normal state. This working point is found to be optimal in terms of energy resolution during the optical characterization. The TES is operated in electrothermal feedback and read out by a SQUID array [28] coupled to the inductance $L = 6$ nH.

The I_{CNT} measurements, as a function of V_{CNT}, are summarized by the black curve of Fig. 3. As can be seen, I_{CNT} exhibits an exponential rise, compatible with the Fowler-Nordheim theory on field emission [29]. Superimposed with red markers is the rate of counts recorded by the TES, which follows the same exponential rise as I_{CNT}, therefore proving that the signals recorded by the TES are due to electrons. The inset in Fig. 3 shows a typical TES signal for $V_{CNT} = 100$ V, characterized by a rise time $\tau_+ \approx 200$ ns and a recovery time $\tau_- \approx 10 \, \mu s$.

A feature of Fowler-Nordheim emission is that the electron current depends on the electric field $|\vec{E}|$, which in our planar configuration is approximated by $|\vec{E}| = V_{CNT}/d$. Moreover, the kinetic energy of these electrons is also determined by V_{CNT}, as shown in Eq. (1). Therefore, in our setup, the signal rate and energy are not independent parameters, as they both depend on V_{CNT}.
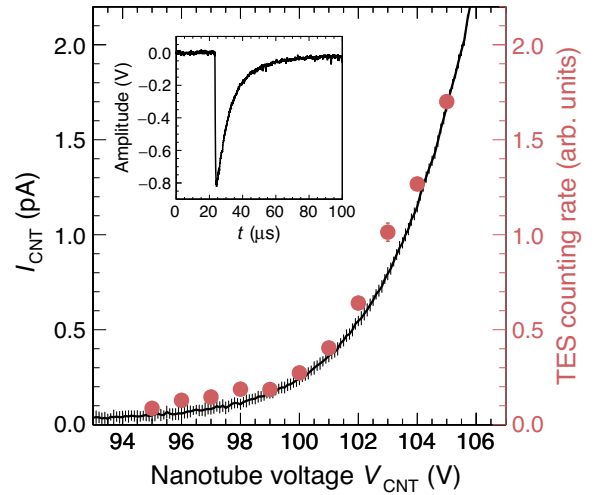

FIG. 3. Current I_{CNT} emitted by the nanotubes (black curve, left vertical scale), as a function of the negative voltage V_{CNT} provided to them, compared with the rate of pulses (red markers, right vertical scale) recorded by the TES. The inset shows a typical TES pulse shape for $V_{CNT} = 100$ V.

The electrons are emitted from an area much larger than the TES, so the heating created by electrons hitting the nearby environment must be considered. In general, the Joule power P_J required to bring the TES to its critical temperature T_C is given by [30]

$$P_J(T_{local}) = I_0^2 R_0(T_{local}) = \kappa(T_C^n - T_{local}^n), \quad (2)$$

where I_0 is the current flowing in the TES; the exponential parameter and the coupling constant of this device
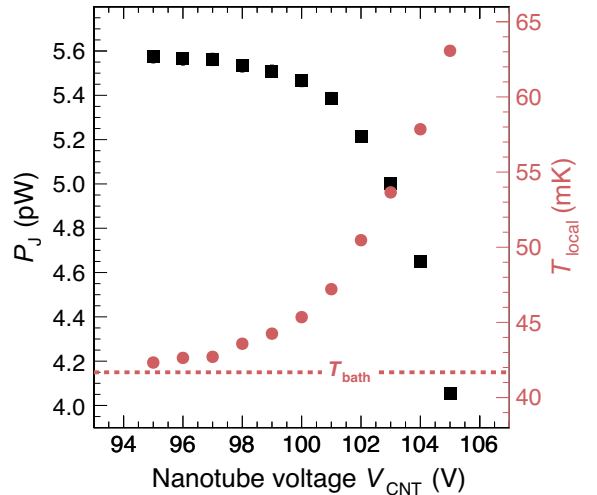

FIG. 4. Power P_J needed to bring the TES to its working point (black markers, left vertical scale) and local temperature T_{local} around the TES device (red markers, right vertical scale) for different values of V_{CNT}. The bath temperature $T_{bath} = 41.7$ mK is indicated by the red dashed line.

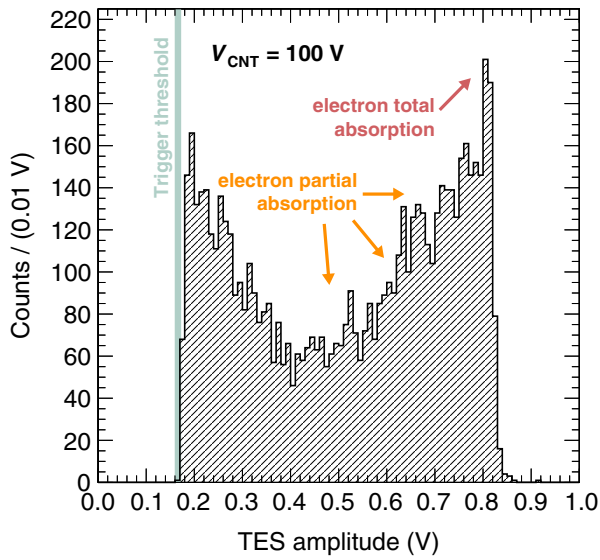FIG. 5. Typical spectrum of TES signal amplitudes, obtained with $V_{CNT} = 100$ V.

FIG. 6. Example fits, for four different values of V_{CNT}, of the high-amplitude peak with the asymmetric Gaussian function.

are respectively measured to be $n = 4.78 \pm 0.07$ and $\kappa = (10 \pm 1) \times 10^{-7}$ W K^{-n}; and T_{local} is the local temperature in proximity of the TES. At low V_{CNT} the electron rate is minimal, and therefore $T_{local} \approx T_{bath}$. As V_{CNT} increases, the rate of electrons and the associated energy deposition in the vicinity of the TES increase, raising T_{local}. This effect is shown in Fig. 4, where the black markers represent P_J, as measured from I_0 and R_0, and the red markers represent T_{local}, as obtained by inverting Eq. (2). As can be seen, when operating the electron source at $V_{CNT} = 105$ V, the local temperature is already $T_{local} > 63$ mK, over 20 mK above T_{bath}. This implies that results at different V_{CNT} values are not rigorously comparable, as the TES operates under different conditions.

For each value of V_{CNT}, the amplitudes of the TES signals are analyzed. A typical spectrum, obtained for $V_{CNT} = 100$ V, is shown in Fig. 5: it presents a high-amplitude peak, corresponding to the full absorption of the electrons in the TES; a marked tail to the left of the peak, due to partial absorption of electrons, most likely due to electrons that fail to be stopped by the thin TES bilayer (45 nm); and a low-amplitude peak, truncated by the trigger threshold of 166 mV, compatible with electrons backscattered out of the TES after exciting an internal mode in the Au layer.

We fit the high-amplitude peaks of these distributions with asymmetric Gaussian functions, described by the peak position μ, and left (σ_L) and right (σ_R) tails. The parameter σ_R is mainly due to the energy resolution of the device. Example fits, for $V_{CNT} = 97, 101, 103$, and 105 V, are shown in Fig. 6.

Figure 7 shows the TES Gaussian energy resolution for fully absorbed electrons (red circular markers) and photons (black square markers) as a function of the particle energy.
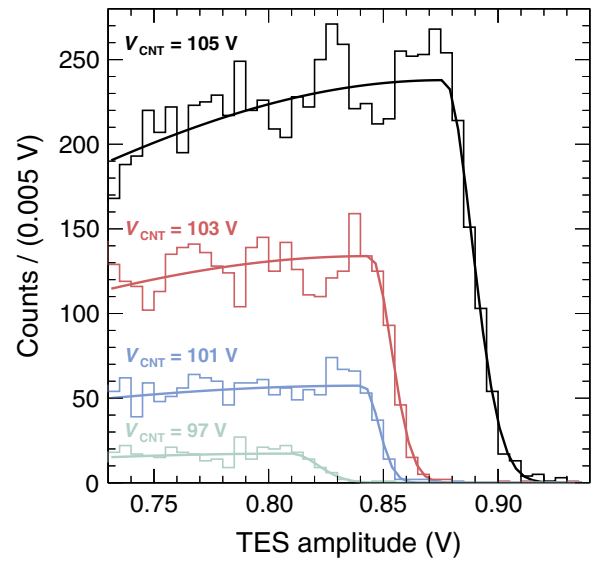
The photon energy resolution is defined as the Gaussian widths of the fit shown in Fig. 2. The electron energy resolution is $\sigma_e = (\sigma_R/\mu) \times E_e$.

The Gaussian energy resolution, for fully absorbed electrons, is measured to be $0.8 < \sigma_e < 1.8$ eV for electrons in the $90 \le E_e \le 101$ eV energy range, and is found to be compatible with that of photons in the same energy range. This is a nontrivial result, as at such low energy these particles have different interactions with matter, and suggests that the heat-based detection mechanism in the TES is the
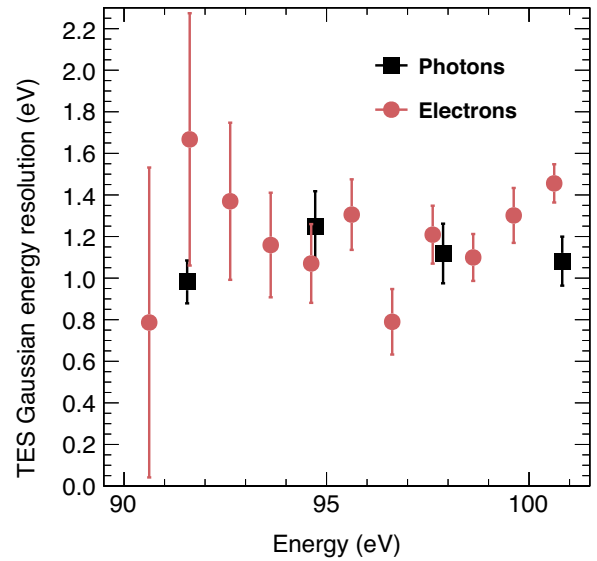

FIG. 7. TES electron energy resolution for photons (black square markers) and fully absorbed electrons (red circular markers) as a function of the particle energy.

same for electrons and photons. This casts optimism on the PTOLEMY target of $\sigma_e = 50$ meV, because this has already been achieved by these devices with photons [4]. Clearly, to develop a high-resolution low-energy electron detector, significant work will be needed to understand the processes that broaden the left side of the absorption peak, and find solutions to limit their impact. Nevertheless, this work marks the beginning of high-resolution electron spectroscopy with TES devices.

[1] K. Irwin, An application of electrothermal feedback for high resolution cryogenic particle detection, Appl. Phys. Lett. **66**, 1998 (1995).

[2] M. Cunningham, J. Ullom, T. Miyazaki, S. Labov, J. Clarke, T. Lanting, A. T. Lee, P. Richards, J. Yoon, and H. Spieler, High-resolution operation of frequency-multiplexed transition-edge photon sensors, Appl. Phys. Lett. **81**, 159 (2002).

[3] K. Hattori, T. Konno, Y. Miura, S. Takasu, and D. Fukuda, An optical transition-edge sensor with high energy resolution, Supercond. Sci. Technol. **35**, 095002 (2022).

[4] L. Lolli, E. Taralli, C. Portesi, E. Monticone, and M. Rajteri, High intrinsic energy resolution photon number resolving detectors, Appl. Phys. Lett. **103**, 041107 (2013).

[5] K. M. Patel, S. Withington, A. G. Shard, D. J. Goldie, and C. N. Thomas, Electron spectroscopy using transition-edge sensors, J. Appl. Phys. **135**, 224504 (2024).

[6] A. Apponi, F. Pandolfi, I. Rago, G. Cavoto, C. Mariani, and A. Ruocco, Absolute efficiency of a two-stage microchannel plate for electrons in the 30–900 eV energy range, Meas. Sci. Technol. **33**, 025102 (2022).

[7] A. Apponi, G. Cavoto, M. Iannone, C. Mariani, F. Pandolfi, D. Paoloni, I. Rago, and A. Ruocco, Response of windowless silicon avalanche photo-diodes to electrons in the 90–900 eV range, JINST **15**, P11015 (2020).

[8] M. Gugiatti, M. Biassoni, M. Carminati, O. Cremonesi, C. Fiorini, P. King, P. Lechner, S. Mertens, L. Pagnanini, M. Pavan, and S. Pozzi, Characterisation of a silicon drift detector for high-resolution electron spectroscopy, Nucl. Instrum. Methods Phys. Res. A: Accel. Spectrom. Detect. Assoc. Equip. **979**, 164474 (2020).

[9] M. Loidl, J. Beyer, L. Bockhorn, C. Enss, S. Kempf, K. Kossert, R. Mariam, O. Nähle, M. Paulsen, P. Ranitzsch, *et al.*, Beta spectrometry with metallic magnetic calorimeters in the framework of the European EMPIR project MetroBeta, Appl. Radiat. Isot. **153**, 108830 (2019).

[10] R. P. Fitzgerald, B. K. Alpert, D. T. Becker, D. E. Bergeron, R. M. Essex, K. Morgan, S. Nour, G. O'Neil, D. R. Schmidt, G. A. Shaw, *et al.*, Toward a new primary standardization of radionuclide massic activity using microcalorimetry and quantitative milligram-scale samples, J. Res. Natl. Inst. Stand. Technol. **126**, 126048 (2021).

[11] M. G. Betti, *et al.*, (PTOLEMY Collaboration), A design for an electromagnetic filter for precision energy measurements at the tritium endpoint, Prog. Part. Nucl. Phys. **106**, 120 (2019).

[12] M. G. Betti, *et al.*, (PTOLEMY Collaboration), Neutrino physics with the PTOLEMY project: active neutrino properties and the light sterile case, J. Cosmol. Astropart. Phys. **2019**, 047 (2019).

[13] A. Apponi, *et al.*, (PTOLEMY Collaboration), Implementation and optimization of the PTOLEMY transverse drift electromagnetic filter, J. Instrum. **17**, P05021 (2022).

[14] C. Pepe, Superconducting transition-edge sensors in tomorrow physics, Nuovo Cimento C **46**, 75 (2023).

[15] E. Monticone, M. Castellino, R. Rocci, and M. Rajteri, Ti/Au ultrathin films for TES application, IEEE Trans. Appl. Supercond. **31**, 1 (2021).

[16] L. Manenti, C. Pepe, I. Sarnoff, T. Ibrayev, P. Oikonomou, A. Knyazev, E. Monticone, H. Garrone, F. Alder, O. Fawwaz, A. J. Millar, K. D. Morå, H. Shams, F. Arneodo, and M. Rajteri, Dark counts in optical superconducting transition-edge sensors for rare-event searches, Phys. Rev. Appl. **22**, 024051 (2024).

[17] E. Monticone, A. M. Rossi, M. Rajteri, R. S. Gonnelli, V. Lacquaniti, and G. Amato, Structural and morphological properties of evaporated SiOx films, Philos. Mag. B **80**, 523 (2000).

[18] E. Schifano, G. Cavoto, F. Pandolfi, G. Pettinari, A. Apponi, A. Ruocco, D. Uccelletti, and I. Rago, Plasma-etched vertically aligned CNTs with enhanced antibacterial power, Nanomaterials **13**, 1081 (2023).

[19] R. P. Yadav, I. Rago, F. Pandolfi, C. Mariani, A. Ruocco, S. Tayyab, A. Apponi, and G. Cavoto, Evaluation of vertical alignment in carbon nanotubes: A quantitative approach, Nucl. Instrum. Methods Phys. Res. A: Accel. Spectrom. Detect. Assoc. Equip. **1060**, 169081 (2024).

[20] F. Sarasini, J. Tirillò, M. Lilli, M. P. Bracciale, P. E. Vullum, F. Berto, G. De Bellis, A. Tamburrano, G. Cavoto, F. Pandolfi, and I. Rago, Highly aligned growth of carbon nanotube forests with in-situ catalyst generation: A route to multifunctional basalt fibres, Compos. B: Eng. **243**, 110136 (2022).

[21] S. Tayyab, A. Apponi, M. G. Betti, E. Blundo, G. Cavoto, R. Frisenda, N. Jiménez-Arévalo, C. Mariani, F. Pandolfi, A. Polimeni, *et al.*, Spectromicroscopy study of induced defects in ion-bombarded highly aligned carbon nanotubes, Nanomaterials **14**, 77 (2024).

[22] W. A. de Heer, A. Châtelain, and D. Ugarte, A carbon nanotube field-emission electron source, Science **270**, 1179 (1995).

[23] I. Lahiri and W. Choi, Interface control: A modified rooting technique for enhancing field emission from multiwall carbon nanotube based bulk emitters, Acta Mater. **59**, 5411 (2011).

[24] V. Semet, V. T. Binh, P. Vincent, D. Guillot, K. Teo, M. Chhowalla, G. Amaratunga, W. Milne, P. Legagneux, and

D. Pribat, Field electron emission from individual carbon nanotubes of a vertically aligned array, Appl. Phys. Lett. **81**, 343 (2002).

[25] P.-H. Lin, C.-L. Sie, C.-A. Chen, H.-C. Chang, Y.-T. Shih, H.-Y. Chang, W.-J. Su, and K.-Y. Lee, Field emission characteristics of the structure of vertically aligned carbon nanotube bundles, Nanoscale Res. Lett. **10**, 1 (2015).

[26] M. Araidai, Y. Nakamura, and K. Watanabe, Field emission mechanisms of graphitic nanostructures, Phys. Rev. B **70**, 245410 (2004).

[27] R. Gomer, Field emission, field ionization, and field desorption, Surf. Sci. **299-300**, 129 (1994).

[28] D. Drung, C. Abmann, J. Beyer, A. Kirste, M. Peters, F. Ruede, and T. Schurig, Highly sensitive and easy-to-use SQUID sensors, IEEE Trans. Appl. Supercond. **17**, 699 (2007).

[29] R. H. Fowler and L. Nordheim, Electron emission in intense electric fields, Proc. R. Soc. Lond. Ser. A-Contain. Pap. Math. Phys. Character **119**, 173 (1928).

[30] K. D. Irwin and G. C. Hilton, in *Cryogenic particle detection* (Springer, Berlin, Germany, 2005), p. 63.